IEICE TRANS. COMMUN., VOL.E104–B, NO.7 JULY 2021

PAPER Special Section on Future Directions of Research and Development on Communication Quality

Graph Laplacian-Based Sequential Smooth Estimator for Three-Dimensional RSS Map

Takahiro MATSUDA[†a)], ***Senior Member***, **Fumie ONO**[††b)], ***and*** **Shinsuke HARA**[†††c)], ***Members***

SUMMARY In wireless links between ground stations and UAVs (Unmanned Aerial Vehicles), wireless signals may be attenuated by obstructions such as buildings. A three-dimensional RSS (Received Signal Strength) map (3D-RSS map), which represents a set of RSSs at various reception points in a three-dimensional area, is a promising geographical database that can be used to design reliable ground-to-air wireless links. The construction of a 3D-RSS map requires higher computational complexity, especially for a large 3D area. In order to sequentially estimate a 3D-RSS map from partial observations of RSS values in the 3D area, we propose a graph Laplacian-based sequential smooth estimator. In the proposed estimator, the 3D area is divided into voxels, and a UAV observes the RSS values at the voxels along a predetermined path. By considering the voxels as vertices in an undirected graph, a measurement graph is dynamically constructed using vertices from which recent observations were obtained and their neighboring vertices, and the 3D-RSS map is sequentially estimated by performing graph Laplacian regularized least square estimation.

key words: *unmanned aerial vehicle, received signal strength, graph Laplacian, least square estimation, sequential estimation*

1. Introduction

Recent technological developments have enabled the use of new infrastructures such as UAVs (Unmanned Aerial Vehicles) in communication networks. So far, a variety of UAV wireless networks such as flying base stations and UAV multihop networks have been studied [1]–[8]. In order to support heavy traffic applications such as high-definition videos or to realize BVLOS (Beyond Visual Line-Of-Sight) flights [9], it is important to design reliable wireless links in the UAV networks. In this regard, there have been many studies on channel measurement and modeling [10]–[16].

There are two types of wireless links in UAV networks, namely air-to-air links between UAVs [10], [11] and ground-to-air links between ground stations and UAVs [12], [14], [17], [18]. Air-to-air links at a sufficiently high altitude can be modeled using a Rician fading channel [10] because there is a direct LOS (Line-Of-Sight) path between the UAVs. On the other hand, NLOS (Non-Line-Of-Sight) paths are used in ground-to-air links because terrestrial obstructions such as buildings between ground stations and UAVs cause shadowing losses [12].

We focus on large-scale fading in ground-to-air links, i.e., path loss and shadowing loss, and try to construct *three-dimensional RSS (Received Signal Strength)* (3D-RSS) maps, which represent a set of RSSs at various reception points in a three-dimensional area. A 3D-RSS map can be obtained by dividing the area into voxels and measuring the RSS at each voxel. Obviously, this is a simple but less cost-effective method.

In this paper, we propose a graph Laplacian-based sequential smooth estimator for 3D-RSS maps. By using the *denoising property* of graph Laplacian [19], [20] and the spatial correlation property of large-scale fading [21], [22], the proposed estimator estimates large-scale fading instead of small-scale fading. In the proposed estimator, a UAV moves along a predetermined path in the three-dimensional area and measures the RSS values on that path. By considering the voxels as vertices in an undirected graph, a *measurement graph* is constructed dynamically using vertices from which recent observations were obtained and their neighboring vertices, and the graph Laplacian is obtained from the measurement graph. The 3D-RSS map is then sequentially estimated by graph Laplacian regularized least square estimation.

The proposed estimator estimates a 3D-RSS map from partial observations of RSS values in the three-dimensional area. Although this approach has been considered in several studies in the literature [23]–[31], which will be reviewed in Sect. 2, we make the following contributions in this paper.

1. Because each measurement graph is constructed using fewer vertices from among all the vertices in the three-dimensional area, the computational cost for estimating the 3D-RSS map is significantly reduced.
2. The positions and postures of UAVs sometimes fluctuate due to wind disturbance; therefore, a finer estimation of the 3D-RSS map does not always provide useful information for reliable ground-to-air links. The proposed estimator is capable of obtaining a rough estimation of the 3D-RSS map by using the smoothing effect of the graph Laplacian.

The remainder of this paper is organized as follows. In Sect. 2, we review some papers related to the RSS map estimation problem. In Sect. 3, we describe the graph Lapla-

Manuscript received August 23, 2020.
Manuscript revised November 21, 2020.
Manuscript publicized January 8, 2021.

[†]The author is with Graduate School of Systems Design, Tokyo Metropolitan University, Hino-shi, 191-0065 Japan.
[††]The author is with National Institute of Information and Communication, Yokosuka-shi, 239-0847 Japan.
[†††]The author is with Graduate School of Engineering, Osaka City University, Osaka-shi, 558-8585 Japan.
a) E-mail: takahiro.m@tmu.ac.jp
b) E-mail: fumie@m.ieice.org
c) E-mail: hara@info.eng.osaka-cu.ac.jp

DOI: 10.1587/transcom.2020CQP0003

cian regularized least square estimation. In Sect. 4, we propose the sequential smooth estimator based on the graph Laplacian-regularized least square. Finally, we evaluate the performance of the proposed scheme with simulation experiments in Sect. 5 and provide our conclusions in Sect. 6.

2. Related Work

RSS maps are useful for designing and managing several wireless communication systems. In [23]–[27], *spectrum cartography* techniques were considered in the context of *cognitive radio*. In cognitive radio networks, secondary users utilize frequency bands without disrupting the connections of primary users. In order to discover vacant frequency bands, spectrum cartography is used to construct RSS maps over a geographical area from RSS values sensed at a certain number of sensors within the area. In [28]–[30], 3D-RSS map estimation techniques for ground-to-air links, which is our target application in this paper, were considered to determine the optimal positions of UAVs. Mostofi [31] utilized spatial cooperative mapping to estimate spatial fields of interest such as the height map of mountains from measurements obtained using UAVs.

In most of the above references, spatial maps were estimated by utilizing their spatial correlation property. In [23], [24], Kriging, a linear spatial interpolation technique was used to estimate the missing values at unobserved locations. In [25], [26], [31], compressive sampling [32] was applied under the assumption that spatial maps are sparse in some transform domains such as Fourier transform and DCT (Discrete Cosine Transform). In [30], by considering a 3D-RSS map as a third-order tensor, the 3D-RSS map was estimated using a low-rank tensor completion technique [33]. In [27], non-parametric estimators from quantized power measurements were proposed using kernel-based learning. In [28], a segmented regression method based on maximum likelihood estimation was proposed. Esrafilian and Gesbert [29] proposed a 3D city map reconstruction algorithm, which uses a different approach from that of other methods. In this algorithm, the users on the ground are classified into LOS and NLOS categories, and the positions and heights of buildings are estimated from the data of user positions.

As mentioned in Sect. 1, our proposed scheme employs a different approach from those mentioned above. It uses graph Laplacian and performs sequential estimation and smooth estimation based on graph Laplacian regularized least square. In order to reduce the computational cost, the proposed scheme performs sequential estimation of 3D-RSS maps. A single UAV moves along a predetermined path and measures the RSS values on that path. A fraction of the 3D-RSS map is estimated at each measurement time, and the whole map is not estimated until the UAV reaches the end of the path. Furthermore, the 3D-RSS map is smoothly estimated by using the properties of the quadratic form of the graph Laplacian. It should be noted that due to the complex structure of the geographical maps, the 3D-RSS maps may have local fluctuations even if there is no small-scale fading effect. The proposed scheme can smooth these local fluctuations.

3. Graph Laplacian Regularized Least Square Estimation

Let $\mathcal{G} = (\mathcal{V}, \mathcal{E})$ denote an undirected graph, where $\mathcal{V} = \{v_n \mid n = 1, 2, \ldots, N\}$ and $\mathcal{E} \subseteq \mathcal{V} \times \mathcal{V}$ represent a set of vertices with the number $N = |\mathcal{V}|$ of nodes and a set of edges, respectively. We define the adjacent matrix $\boldsymbol{A} = [a_{i,j}]_{0 \le i,j \le N}$ of $\mathcal{G}$ as a non-negative matrix, where $a_{i,j}$ ($a_{i,j} \ge 0$) represents the weight of edge $(i, j) \in \mathcal{E}$. The degree matrix $\boldsymbol{D} = \mathrm{diag}\{d_1, d_2, \ldots, d_N\}$ is a diagonal matrix whose i-th element ($i = 1, 2, \ldots, N$) is given by

$$d_i = \sum_{j=1}^{N} a_{i,j}.$$

Then, the graph Laplacian $\boldsymbol{L}$ is given by $\boldsymbol{L} = \boldsymbol{D} - \boldsymbol{A}$ [34], [35].

Let a real vector $\boldsymbol{x} = (x_1\ x_2\ \cdots\ x_N)^\top$ denote a *graph signal*, where the n-th element x_n of $\boldsymbol{x}$ is associated with vertex $v_n \in \mathcal{V}$ and $\top$ denotes the transpose operator. The quadratic form $\boldsymbol{x}^\top \boldsymbol{L}\boldsymbol{x}$ is represented by

$$\boldsymbol{x}^\top \boldsymbol{L}\boldsymbol{x} = \sum_{(n_1,n_2)\in\mathcal{E}} a_{n_1,n_2}(x_{n_1} - x_{n_2})^2. \tag{1}$$

Because $a_{i,j} \ge 0$, $\boldsymbol{L}$ is non-negative definite. We now consider a linear inverse problem to estimate $\boldsymbol{x}$ from a system of equations:

$$\boldsymbol{y} = \boldsymbol{B}\boldsymbol{x},$$

where $\boldsymbol{y} = (y_1\ y_2\ \cdots\ y_M)^\top$ and $\boldsymbol{B} \in \mathbb{R}^{M\times N}$ denote the *measurement vector* and the *measurement matrix*, respectively. We assume $M < N$, which means that the above inverse problem is *under-determined*, and estimate $\boldsymbol{x}$ by optimizing the *graph Laplacian regularized least square* problem:

$$\min_{\boldsymbol{x}} \left\{ \|\boldsymbol{y} - \boldsymbol{B}\boldsymbol{x}\|_2^2 + \lambda \boldsymbol{x}^\top \boldsymbol{L}\boldsymbol{x} \right\}, \tag{2}$$

where λ ($\lambda > 0$) denotes a weighting parameter. $\|\boldsymbol{z}\|_2$ represents the ℓ_2 norm of vector $\boldsymbol{z}$, and for $\boldsymbol{z} = (z_1\ z_2\ \cdots\ z_N)^\top \in \mathbb{R}^N$, $\|\boldsymbol{z}\|_2$ is given by

$$\|\boldsymbol{z}\|_2 = \sqrt{\sum_{n=1}^{N} z_n^2}$$

By solving (2), the estimation $\hat{\boldsymbol{x}}$ of $\boldsymbol{x}$ is obtained as follows:

$$\hat{\boldsymbol{x}} = \left(\boldsymbol{B}^\top \boldsymbol{B} + \lambda \boldsymbol{L}\right)^{-1} \boldsymbol{B}^\top \boldsymbol{y}.$$

From (1), the quadratic form $\boldsymbol{x}^\top \boldsymbol{L}\boldsymbol{x}$ is small when the graph signal $\boldsymbol{x}$ includes elements that have comparable values at neighboring vertices. Therefore, $\hat{\boldsymbol{x}}$ is a smooth estimator of $\boldsymbol{x}$.

4. Graph Laplacian-Based Sequential Smooth Estimator

4.1 System Model

In ground-to-air links, the wireless signal transmitted from a ground station is received by a UAV in air, and in addition to the path loss, the signal is attenuated by obstructions such as buildings (i.e., shadowing effect) as shown in Fig. 1. The shadowing effect exhibits spatial correlation [22]; that is, the wireless signals received at nearby locations have comparable powers. By using this property, the proposed scheme estimates the RSS map from partially observed RSSs as shown in Fig. 2. Suppose that there is one UAV and one ground station in an area. The UAV flies within the area and measures the RSSs at several locations on its path. From the measurements, the RSS map of the area is sequentially estimated. Although we consider a simple situation with one UAV and one ground station in this study, we can apply the proposed scheme to situations with multiple UAVs and ground stations.

Let $\mathcal{R} \subset \mathbb{R}^p$ denote a P-dimensional *sensing area* ($P \leq 3$). We define $Z(\boldsymbol{r})$ as the RSS at location $\boldsymbol{r} \in \mathcal{R}$. We divide $\mathcal{R}$ into N voxels $\mathcal{Q} = \{q_1, q_2, \ldots, q_N\}$, where each voxel q_n has a size of $\delta^P[\mathrm{m}^P]$ ($\delta > 0$) and $\boldsymbol{c}(q_n) \in \mathcal{R}$ represents the location of the center of q_n. We assume that $Z(\boldsymbol{r})$ is approximately constant within each voxel and define the *RSS vector* $\boldsymbol{z} = (Z(\boldsymbol{c}(q_1))\ Z(\boldsymbol{c}(q_2))\ \cdots\ Z(\boldsymbol{c}(q_N)))^\top$.

4.2 Construction of Measurement Graph

Let $\mathcal{G} = (\mathcal{V}, \mathcal{E})$ denote an undirected graph constructed from $\mathcal{Q}$, where $v_n \in \mathcal{V}$ corresponds to $q_n \in \mathcal{Q}$ ($n = 1, 2, \ldots, N$). To avoid confusion, hereinafter, we refer to $v_n \in \mathcal{V}$ and the UAV used to measure RSSs as a *vertex* and *node*, respectively. Let $\mathrm{dist}(\boldsymbol{r}_i, \boldsymbol{r}_j)$ represent the distance between $\boldsymbol{r}_i$ and $\boldsymbol{r}_j$ defined as $\mathrm{dist}(\boldsymbol{r}_i, \boldsymbol{r}_j) = \|\boldsymbol{r}_i - \boldsymbol{r}_j\|_2$. We set $(v_n, v_{n'}) \in \mathcal{E}$ if $\mathrm{dist}(\boldsymbol{c}(q_n), \boldsymbol{c}(q_{n'})) \leq d_{\mathrm{th}}$ ($d_{\mathrm{th}} > 0$). $\boldsymbol{A} = [a_{i,j}]_{1 \leq i,j \leq N}$ represents an adjacent matrix of $\mathcal{G}$, and the (i, j)-th element $a_{i,j}$ of $\boldsymbol{A}$ is set to $a_{i,j} = 1$ if $(v_i, v_j) \in \mathcal{E}$ and $a_{i,j} = 0$ otherwise.

Let m ($m = 1, 2, \ldots$) denote the *measurement times*. We define the *measurement graph* $\mathcal{G}(m) = (\mathcal{V}(m), \mathcal{E}(m))$ at measurement time m, where $\mathcal{V}(m) \subseteq \mathcal{V}$ and $\mathcal{E}(m) \subseteq \mathcal{E}$, and $\boldsymbol{A}(m)$ denotes the adjacent matrix of $\mathcal{G}(m)$. The node obtains one measurement at each measurement time.

$\mathcal{G}(m)$ is updated at each measurement time as follows. Let $q(m) \in Q$ denote the voxel in which the node exists at measurement time m, which is referred to as a *measurement point*. The *set* $\mathcal{Q}_{\mathrm{M}}(m)$ *of measurement points* at measurement time m is defined as

$$\mathcal{Q}_{\mathrm{M}}(m) = \{q(m-k) \in \mathcal{Q} \mid k = 0, 1, \ldots K-1\},$$

where $K = |\mathcal{Q}_{\mathrm{M}}(m)|$ for $m = 1, 2, \ldots$, and the *set* $\mathcal{Q}_{\mathrm{N}}(m)$ *of neighboring points* is defined as

$$\mathcal{Q}_{\mathrm{N}}(m) = \{q_n \in \mathcal{Q} \mid \mathrm{minhop}(v_n, v_m) \leq H_{\mathrm{th}},$$

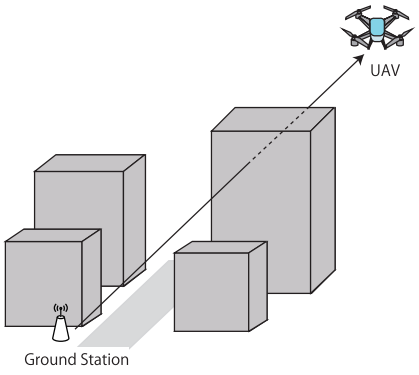

Fig. 1 Ground-to-Air communication.

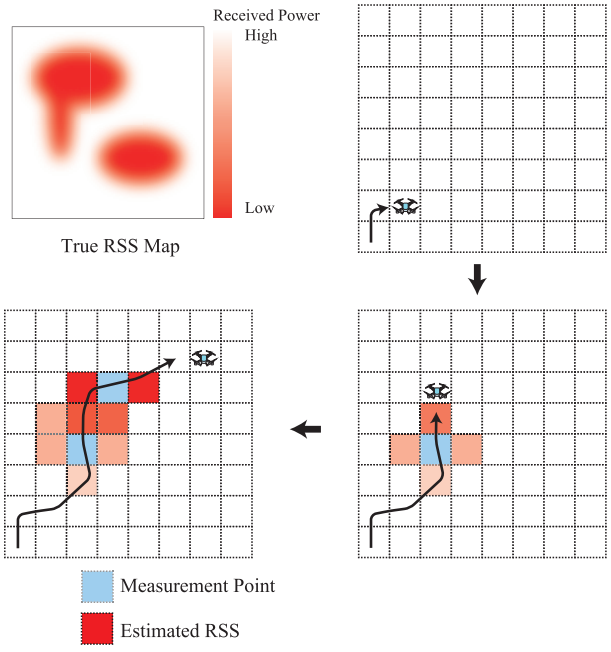

Fig. 2 Sequential estimation of RSS map. A UAV measures the RSSs at several locations on its path, and the 3D-RSS map is sequentially estimated from these measurements.

$$\text{for } \forall q_m \in \mathcal{Q}_{\mathrm{M}}, q_m \neq q_n\},$$

where $\mathrm{minhop}(v_n, v_m)$ is the minimum hop between v_n and v_m on graph $\mathcal{G}$. Namely, $\mathcal{Q}_{\mathrm{N}}(m)$ represents the set of voxels around those in $\mathcal{Q}_{\mathrm{M}}(m)$. Let $\mathcal{V}_{\mathrm{M}}(m) \subset \mathcal{V}$ and $\mathcal{V}_{\mathrm{N}}(m) \subset \mathcal{V}$ denote the sets of vertices corresponding to $\mathcal{Q}_{\mathrm{M}}(m)$ and $\mathcal{Q}_{\mathrm{N}}(m)$, respectively, and $N(m)$ denotes the number of voxels in $\mathcal{Q}_{\mathrm{M}}(m) \cup \mathcal{Q}_{\mathrm{N}}(m)$. $\mathcal{V}(m)$ is then given by $\mathcal{V}(m) = \mathcal{V}_{\mathrm{M}}(m) \cup \mathcal{V}_{\mathrm{N}}(m)$, and $\mathcal{G}(m)$ is defined as the vertex-induced subgraph of $\mathcal{G}$ on $\mathcal{V}(m)$, where $\mathcal{E}(m)$ consists of edges whose endpoints are in $\mathcal{V}(m)$ [36]. Figure 3 shows an example of a measurement graph for a 2-dimensional region $\mathcal{R}$.

The node measures the RSS value $y_m = Z(\boldsymbol{c}(q(m)))$ at measurement time m. We define the *measurement vector* $\boldsymbol{y}(m)$ at measurement time m, consisting of RSS values measured at the measurement points in $\mathcal{Q}_{\mathrm{M}}(m)$, that is,

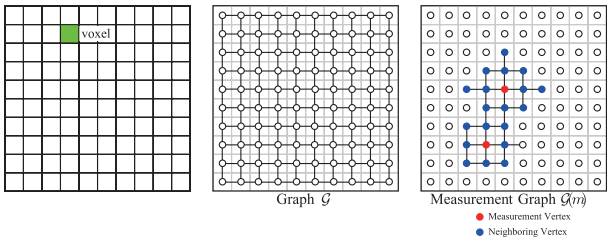

Fig. 3 Example of measurement graph for 2-dimensional sensing area. The left figure shows the voxels within the sensing area $\mathcal{R}$. The middle figure shows the graph $\mathcal{G}$ for $d_{\text{th}} = \delta$. The right figure shows the measurement graph $\mathcal{G}(m)$ with $H_{\text{th}} = 2$.

$\boldsymbol{y}(m) = (y_m\ y_{m-1}\ \cdots\ y_{m-K+1})^\top$. We also define the *temporal RSS vector* $\boldsymbol{x}(m)$ at measurement time m as

$$\boldsymbol{x}(m) = \left(Z(\boldsymbol{c}(q_{i_1}))\ Z(\boldsymbol{c}(q_{i_2}))\ \cdots\ Z(\boldsymbol{c}(q_{i_{N(m)}}))\right)^\top,$$

where $q_{i_j} \in \mathcal{Q}_{\text{M}}(m) \cup \mathcal{Q}_{\text{N}}(m)$ $(i_j \in \{1, 2, \ldots, N\}, j = 1, 2, \ldots, N(m))$. The relationship between $\boldsymbol{y}(m)$ and $\boldsymbol{x}(m)$ can be formulated as $\boldsymbol{y}(m) = \boldsymbol{F}(m)\boldsymbol{x}(m)$, where $\boldsymbol{F}(m) \in \{0, 1\}^{K \times N(m)}$ and the (k, l)-th element $f_{k,l}$ in $\boldsymbol{F}(m)$ $(k = 1, 2, \ldots, K, l = 1, 2, \ldots, N(m))$ is set to $f_{k,l} = 1$ if $q(m - k + 1) = q_{i_l}$, and $f_{k,l} = 0$ otherwise. Furthermore, the relationship between $\boldsymbol{x}(m)$ and $\boldsymbol{z}$ is formulated as $\boldsymbol{x}(m) = \boldsymbol{H}(m)\boldsymbol{z}$, where $\boldsymbol{H}(m) \in \{0, 1\}^{N(m) \times N}$ and the (l, n)-th element $h_{l,n}$ $(l = 1, 2, \ldots, N(m), n = 1, 2, \ldots, N)$ in $\boldsymbol{H}(m)$ is set to $h_{l,n} = 1$ if $q_{i_l} = q_n$ and $h_{l,n} = 0$ otherwise. We then obtain the following relationship:

$$\boldsymbol{y}(m) = \boldsymbol{F}(m)\boldsymbol{x}(m) = \boldsymbol{F}(m)\boldsymbol{H}(m)\boldsymbol{z}.$$

Note that for each row in $\boldsymbol{H}(m)$, there is only one element with 1. Suppose that $h_{\tilde{l},\tilde{n}} = 1$ in $\boldsymbol{H}(m)$. We then define a function $id(m, l)$ to identify the element as follows: $id(m, \tilde{l}) = \tilde{n}$. Figure 4 shows the relationship between RSS vector $\boldsymbol{z}$, temporal RSS vector $\boldsymbol{x}(m)$, and measurement vector $\boldsymbol{y}(m)$.

4.3 Sequential Estimation

Our proposed RSS map estimator estimates the RSS vector $\boldsymbol{z}$ sequentially with $\{\boldsymbol{y}(m) \mid m = 1, 2, \ldots\}$. When $\boldsymbol{y}(m)$ is obtained, the proposed estimator estimates $\boldsymbol{x}(m)$ by using the graph Laplacian $\boldsymbol{L}(m)$ of $\mathcal{G}(m)$ and obtains the estimated vector $\hat{\boldsymbol{z}} = (\hat{z}_1\ \hat{z}_2\ \cdots\ \hat{z}_N)^\top$ of $\boldsymbol{z}$ by replacing some elements in $\hat{\boldsymbol{z}}$ with those in $\hat{\boldsymbol{x}}(m) = (\hat{x}_1(m)\ \hat{x}_2(m)\ \cdots\ \hat{x}_{N(m)}(m))^\top$, which is an estimated vector of $\boldsymbol{x}(m)$. The measurement graph $\mathcal{G}(m)$ is updated during each measurement time, and $\mathcal{Q}_{\text{M}}(m) \cap \mathcal{Q}_{\text{M}}(m-1) \neq \emptyset$ $(m \geq 2)$, which means that $\mathcal{G}(m)$ and $\mathcal{G}(m-1)$ share some vertices. Therefore, when $\boldsymbol{y}(m)$ is obtained, the RSS values at some voxels may have already been estimated at some measurement times m' $(m' < m)$. In the proposed estimator, we utilize these estimated RSS values as prior information to estimate the RSS values at measurement time m.

Let $\boldsymbol{S}(m) = \text{diag}(s_1\ s_2\ \cdots\ s_{N(m)})$ denote a diagonal matrix containing voxels that have already been estimated at least once before the measurement time m. Namely, s_n is set to $s_n = 1$ if $x_n(m) = Z(\boldsymbol{c}(q_{i_n}))$ was estimated at measurement time m' $(m' < m)$, and $s_n = 0$ otherwise. Given $\boldsymbol{y}(m)$, $\boldsymbol{F}(m)$, $\boldsymbol{H}(m)$, $\boldsymbol{L}(m)$, and $\boldsymbol{S}(m)$, $\boldsymbol{x}(m)$ is estimated by solving the following optimization problem:

$$\min_{\boldsymbol{x}(m)} \Big\{ \|\boldsymbol{y}(m) - \boldsymbol{F}(m)\boldsymbol{x}(m)\|_2^2 + \lambda \boldsymbol{x}(m)^\top \boldsymbol{L}(m)\boldsymbol{x}(m) + \mu \left\|\boldsymbol{S}(m)\left(\boldsymbol{x}(m) - \boldsymbol{H}(m)\hat{\boldsymbol{z}}\right)\right\|_2^2 \Big\},$$

where $\lambda > 0$ and $\mu \geq 0$. Because this is a kind of regularized least square problem, we can easily obtain $\hat{\boldsymbol{x}}(m)$ as follows:

$$\hat{\boldsymbol{x}}(m) = \left(\boldsymbol{F}(m)^\top \boldsymbol{F}(m) + \lambda \boldsymbol{L}(m) + \mu \boldsymbol{S}(m)\right)^{-1} \cdot \left(\boldsymbol{F}(m)^\top \boldsymbol{y}(m) + \mu \boldsymbol{S}(m)\boldsymbol{H}(m)\hat{\boldsymbol{z}}\right), \tag{3}$$

if $(\boldsymbol{F}(m)^\top \boldsymbol{F}(m) + \lambda \boldsymbol{L}(m) + \mu \boldsymbol{S}(m))$ is a non-singular matrix.

In order to prove the non-singularity of the matrix, we introduce the following lemma:

Lemma 1 (Lemma 14.2.4 in [37]): Let $\boldsymbol{A}$ and $\boldsymbol{B}$ represent square matrices. If either $\boldsymbol{A}$ or $\boldsymbol{B}$ is positive definite and the other is non-negative definite, then $\boldsymbol{A} + \boldsymbol{B}$ is positive definite.

From this lemma, we have the following theorem:

Theorem 1: For $\lambda > 0$ and $\mu \geq 0$, $\boldsymbol{F}(m)^\top \boldsymbol{F}(m) + \lambda \boldsymbol{L}(m) + \mu \boldsymbol{S}(m)$ is a positive definite matrix. Therefore, $(\boldsymbol{F}(m)^\top \boldsymbol{F}(m) + \lambda \boldsymbol{L}(m) + \mu \boldsymbol{S}(m))^{-1}$ always exists.

Proof: Because $\boldsymbol{S}(m) = \text{diag}(s_1\ s_2\ \cdots\ s_N)$ is a diagonal matrix with $s_n \in \{0, 1\}$ $(n = 1, 2, \ldots, N)$, $\boldsymbol{S}(m)$ is a non-negative matrix. Let $\boldsymbol{x}$ denote a non-null real vector (i.e., $\boldsymbol{x} \neq \boldsymbol{0}$) with length $N(m)$. From (1), $\boldsymbol{L}(m)$ is non-negative definite for every $\boldsymbol{x} = (x_1\ x_2\ \cdots\ x_{N(m)})^\top$, and $\boldsymbol{x}^\top \boldsymbol{L}(m)\boldsymbol{x} = 0$ if and only if $x_1 = x_2 = \cdots = x_{N(m)}$. Suppose that $\boldsymbol{x} = \alpha \boldsymbol{1} = (\alpha\ \alpha\ \cdots\ \alpha)^\top$ for $\alpha \neq 0$. From the definition of $\boldsymbol{F}(m)$, $\boldsymbol{F}(m)^\top \boldsymbol{F}(m) = \text{diag}(f'_1\ f'_2\ \cdots\ f'_{N(m)})$, where $f'_l = 1$ $(l = 1, 2, \ldots, N(m))$ if $f_{k,l} = 1$ for $\exists k \in \{1, 2, \ldots, K\}$, and $f'_l = 0$

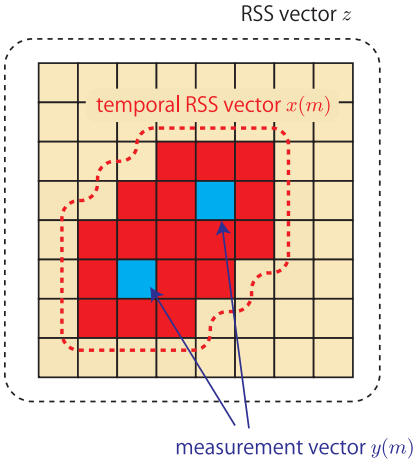

Fig. 4 Relationship between RSS vector $\boldsymbol{z}$, temporal RSS vector $\boldsymbol{x}(m)$, and measurement vector $\boldsymbol{y}(m)$. $\boldsymbol{z}$ contains RSS values at all voxels. $\boldsymbol{x}(m)$ contains RSS values at measurement points and their neighboring points. $\boldsymbol{y}(m)$ contains RSS values at measurement points.

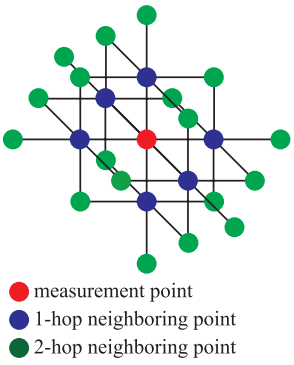

Fig. 5 Example of a basic set containing a measurement vertex and its neighboring vertices for $H_{\text{th}} = 2$.

otherwise. Then, $\boldsymbol{x}^\top \boldsymbol{F}(m)^\top \boldsymbol{F}(m)\boldsymbol{x} > 0$. Therefore, if $\lambda > 0$, $\boldsymbol{F}(m)^\top \boldsymbol{F}(m) + \lambda \boldsymbol{L}(m)$ is a positive definite matrix for every real vector $\boldsymbol{x}$, and from the lemma, $\boldsymbol{F}(m)^\top \boldsymbol{F}(m) + \lambda \boldsymbol{L}(m) + \mu \boldsymbol{S}(m)$ is positive definite for $\lambda > 0$ and $\mu \geq 0$. □

4.4 Sampling

Sampling involves assigning measurement points to some vertices to determine $\mathcal{V}_{\text{M}}(m)$. In the proposed estimator, some vertices may not be in any measurement graph if they are included in neither $\mathcal{V}_{\text{M}}(m)$ nor $\mathcal{V}_{\text{N}}(m)$ for $\forall m$. Therefore, we propose a sampling scheme to avoid these missing vertices.

We define a *basic set* $\mathcal{U}(v)$ for $v \in \mathcal{V}$ as

$$\mathcal{U}(v) = \{u \in \mathcal{V} \mid \text{minhop}(u, v) \leq H_{\text{th}}\}.$$

That is, $\mathcal{U}(v)$ includes the vertex v as well as the vertices within H_{th} hops. Figure 5 shows an example of a basic set $U(v)$ for $H_{\text{th}} = 2$.

The objective of sampling is to find a set $\tilde{V}$ of vertices such that the union of the basic sets of the vertices cover the set $\mathcal{V}$. We can consider an optimization problem to find the minimum number of measurement points as follows:

$$\min_{\tilde{\mathcal{V}}} |\tilde{\mathcal{V}}| \quad \text{subject to} \bigcup_{v \in \tilde{\mathcal{V}}} \mathcal{U}(v) = \mathcal{V}.$$

This problem can be regarded as a *minimum set covering problem*, which is known to be an *NP*-hard problem [38, Sect. 16.1].

Therefore, we propose a heuristic sampling algorithm to find $\tilde{\mathcal{V}}$ as follows. Without loss of generality, we assume that the dimension p of the sensing area $\mathcal{R}$ is $p = 3$ and that $\mathcal{R}$ is composed of N_{L} two-dimensional layers, where each layer contains voxels placed at the same height. Let $\mathcal{R}^{(l)} \subset \mathbb{R}^p$ denote the sensing area in the l-th layer. Figure 6 shows an example of the measurement points obtained using the proposed sampling scheme for $N_{\text{th}} = 2$ and $N_{\text{L}} = 2$.

1. Find the minimum rectangular area $\mathcal{R}_{\min}$ covering $\mathcal{R}^{(l)}$ for $\forall l = 1, 2, \ldots, N_{\text{L}}$, and set the *virtual area* $\tilde{\mathcal{R}}^{(l)}$ in the l-th layer as $\tilde{\mathcal{R}}^{(l)} = \mathcal{R}_{\min}$ (Fig. 6(a)).
2. Divide $\tilde{\mathcal{R}}^{(l)}$ ($l = 1, 2, \ldots, N_{\text{L}}$) into a set $\tilde{\mathcal{Q}}^{(l)}$ containing voxels having the same size δ^p, and assign a vertex to each voxel (Fig. 6(b)). Let $\tilde{\mathcal{V}}^{(l)}$ denote the set of vertices on the l-th layer and $\mathcal{V}^{(l)} \subseteq \tilde{\mathcal{V}}^{(l)}$ denote the set of vertices within $\mathcal{R}^{(l)}$. Because each virtual area is rectangular, the vertices on each layer are placed on a grid. We assume that there are $N_1 N_2$ vertices on each layer, representing the (i, j)-th vertex ($i = 1, 2, \ldots, N_1$, $j = 1, 2, \ldots, N_2$) on the l-th layer with $v_{i,j}^{(l)}$.
3. Set the set $\tilde{\mathcal{Q}}_{\text{M}}^{(l)}$ of measurement points in the virtual area on the l-th layer as shown in (4) (Fig. 6(c)).
4. Set the set $\mathcal{Q}_{\text{M}}^{(l)}$ of measurement points in the l-the layer and $\mathcal{Q}_M$ as

$$\mathcal{Q}_{\text{M}}^{(l)} = \tilde{\mathcal{Q}}_{\text{M}}^{(l)} \cap \mathcal{Q}^{(l)}, \quad \mathcal{Q}_M = \bigcup_{l=1}^{N_{\text{L}}} \mathcal{Q}_{\text{M}}^{(l)}$$

   where $\mathcal{Q}^{(l)}$ denotes the set of voxels corresponding to $\mathcal{V}^{(l)}$ (Fig. 6(d)).
5. Obtain the set $\bar{\mathcal{Q}}$ of *uncovered points* in $\bar{\mathcal{Q}} := \mathcal{Q} \setminus \{\bigcup_{l=1}^{N_{\text{L}}} (\mathcal{Q}_{\text{M}}^{(l)} \cup \mathcal{Q}_{\text{N}}^{(l)})\}$, which are vertices included in neither $\mathcal{Q}_{\text{M}}^{(l)}$ nor $\mathcal{Q}_{\text{N}}^{(l)}$ for $\forall l = 1, 2, \ldots, N_{\text{L}}$ (Fig. 6(d)).
6. If $\bar{\mathcal{Q}} \neq \emptyset$, find $q \in \bar{\mathcal{Q}}$ such that the maximum number of vertices in $\bar{\mathcal{Q}}$ is covered by the basic set $U(q)$, and set $\mathcal{Q}_{\text{M}} := \mathcal{Q}_{\text{M}} \cup \{q\}$ (Fig. 6(e)).
7. Repeat step 6) until $\bar{\mathcal{Q}} = \emptyset$.

4.5 Path Establishment

From $\mathcal{Q}_{\text{M}}$, a path along which the UAV node moves is established. On each layer, one path that visits all the measurement points and has the minimum path length is established as shown in Fig. 7. We define a path $path^{(l)}$ on the l-th layer as

$$path^{(l)} = \left\{ q_{i_1}, q_{i_2}, \ldots, q_{i_{N_{\text{path}}^{(l)}}} \right\},$$

where $N_{\text{path}}^{(l)} = |\mathcal{Q}_{\text{M}}^{(l)}|$, and $[i_1, i_2, \ldots, i_{N_{\text{path}}}]$ is a permutation of $[1, 2, \ldots, N_{\text{path}}]$. We also define the length $\text{len}(\text{path}^{(l)})$ of $path^{(l)}$ as

$$\text{len}(\text{path}^{(l)}) = \sum_{j=1}^{N_{\text{path}^{(l)}}} \text{minhop}(q_{i_j}, q_{i_{j+1}}),$$

where $i_{N_{\text{path}}^{(l)}+1} = i_1$. The problem of finding a path with the minimum length is equivalent to the *travelling salesman problem (TSP)*, which is a typical *NP*-hard problem [38, Theorem 15.43.]. In the proposed estimator, we solve this problem using the *Genetic Algorithm (GA)*.

4.6 Computational Cost

When the *LUP decomposition* is used, the computational

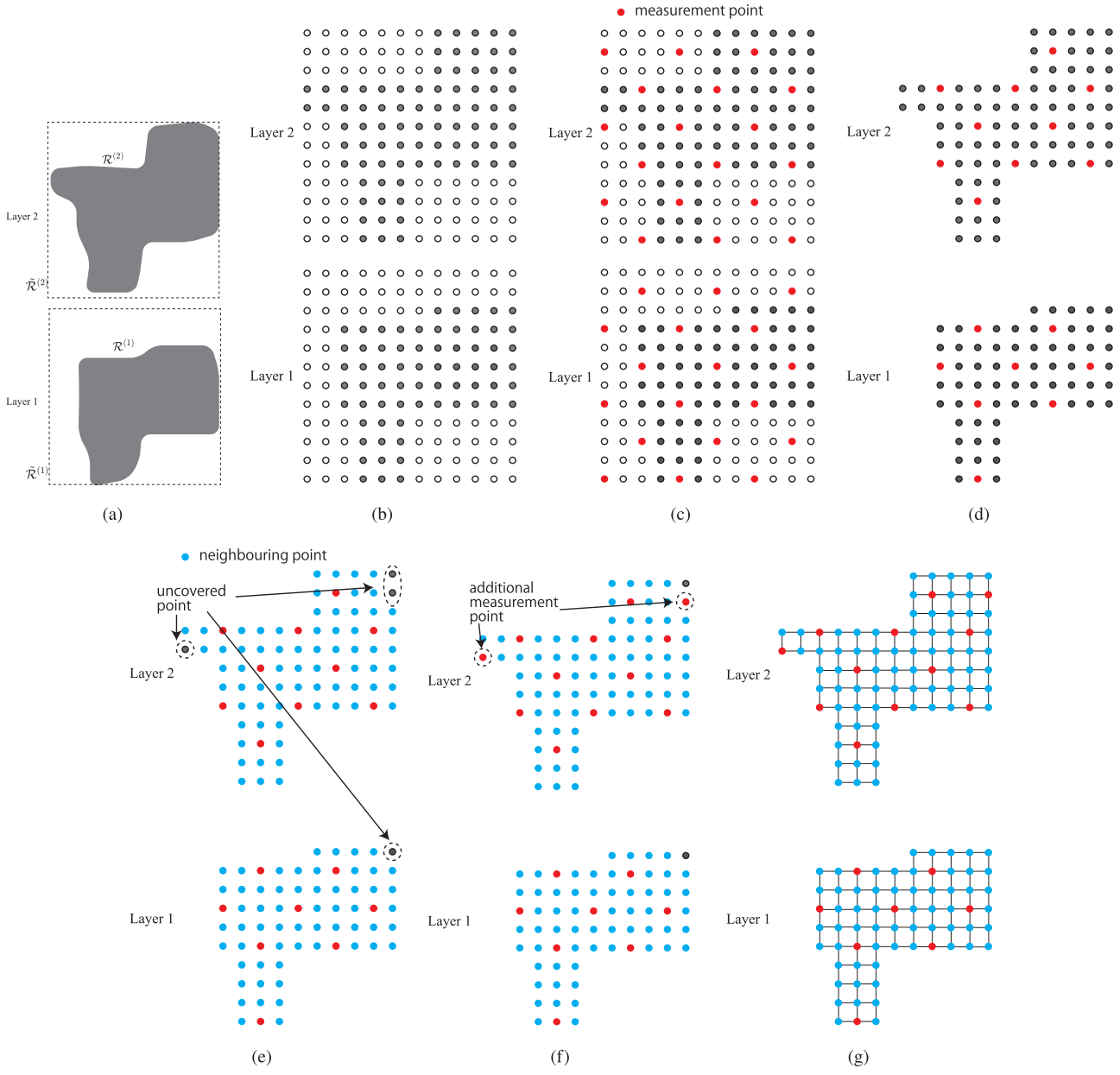

Fig. 6 Example of sampling for $H_{\mathrm{th}} = 2$ and $N_{\mathrm{L}} = 2$. (a) The virtual area $\tilde{\mathcal{R}}^{(l)}$ ($l = 1, 2, \ldots, N_{\mathrm{L}}$ is set in the l-th layer. (b) A vertex is assigned to each voxel. (c) The set $\tilde{\mathcal{Q}}^{(l)}$ of measurement points is set to the vertices in $\tilde{\mathcal{V}}^{(l)}$. (d) The set $\mathcal{Q}^{(l)}$ is obtained from $\tilde{\mathcal{Q}}^{(l)}$. (e) The set $\bar{\mathcal{Q}}$ of uncovered points, which are vertices included in neither $\mathcal{Q}_{\mathrm{M}}^{(l)}$ nor $\mathcal{Q}_{\mathrm{N}}^{(l)}$, is obtained. (f) The measurement points are added to cover the uncovered points. (g) Finally, a measurement graph is obtained.

$$\tilde{\mathcal{Q}}_{\mathrm{M}}^{(l)} = \begin{cases} \left\{ v^{(l)}_{2(i-1)H_{\mathrm{th}}+1,2(j-1)H_{\mathrm{th}}+1} \,\middle|\, i = 1,2,\ldots,\left\lfloor \frac{N_1-1}{2H_{\mathrm{th}}} \right\rfloor, j = 1,2,\ldots,\left\lfloor \frac{N_2-1}{2H_{\mathrm{th}}} \right\rfloor \right\} \\ \quad \cup \left\{ v^{(l)}_{(2i-1)H_{\mathrm{th}}+1,(2j-1)H_{\mathrm{th}}+1} \,\middle|\, i = 1,2,\ldots,\left\lfloor \frac{N_1+H_{\mathrm{th}}-1}{2H_{\mathrm{th}}} \right\rfloor, j = 1,2,\ldots,\left\lfloor \frac{N_2+H_{\mathrm{th}}-1}{2H_{\mathrm{th}}} \right\rfloor \right\} & \text{for } l = 1,3,\ldots \\ \left\{ v^{(l)}_{(2i-1)H_{\mathrm{th}}+1,(2j-1)H_{\mathrm{th}}+1} \,\middle|\, i = 1,2,\ldots,\left\lfloor \frac{N_1-1}{2H_{\mathrm{th}}} \right\rfloor, j = 1,2,\ldots,\left\lfloor \frac{N_2+H_{\mathrm{th}}-1}{2H_{\mathrm{th}}} \right\rfloor \right\} \\ \quad \cup \left\{ v^{(l)}_{2(i-1)H_{\mathrm{th}}+1,2(j-1)H_{\mathrm{th}}+1} \,\middle|\, i = 1,2,\ldots,\left\lfloor \frac{N_1+H_{\mathrm{th}}-1}{2H_{\mathrm{th}}} \right\rfloor, j = 1,2,\ldots,\left\lfloor \frac{N_2-1}{2H_{\mathrm{th}}} \right\rfloor \right\} & \text{for } l = 2,4,\ldots \end{cases} \tag{4}$$

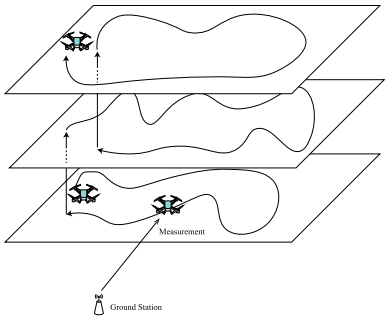

Fig. 7 By means of GA (genetic algorithm), a path that visits all the measurement points has the minimum path length is established.

cost to solve a system $\boldsymbol{y} = \boldsymbol{A}\boldsymbol{x}$ of n linear equations and n unknowns is $\Theta(n^3)$ [39]. Therefore, the computational cost to compute (3) is given by $\Theta(N^3(m))^{\dagger}$. In the simulation experiment in Sect. 5, we will use the 3D-RSS map with $N = 2616$ voxels. As shown in Fig. 5, there are 24 neighboring points when $H_{\text{th}} = 2$. Therefore, in the proposed estimator for $H_{\text{th}} = 2$ and $K = 4$, the measurement graph $\mathcal{G}(m)$ has at most $N(m) = 25 \times K = 100$ vertices, which means that the computational cost is significantly reduced by the sequential estimation.

Note that the above discussion excludes the computational cost of the path establishment, while GA requires a heavy computational cost. The reason is that the path length is not an important factor in the estimation capability of the proposed estimator, which indicates that we can use other heuristic algorithms for path establishment. However, if we need to consider the battery consumption of the UAV, the path length would be an important factor to design the proposed estimator.

5. Performance Evaluation

In this section, we evaluate the performance of the proposed estimator using simulation experiments.

5.1 Simulation Setup

Figure 8(a) shows the 3D city map, which is used to obtain the true 3D-RSS map and find paths in the simulation experiments, and Fig. 8(b) shows the city map projected onto a 2D space. In the map, one ground station is deployed with an antenna height of 1.5 [m]. Figures 8(c), 8(d), and 8(e) show the 3D-RSS map obtained using WinProp [40], which is a ray-tracing wireless propagation simulator. The 3D-RSS map has three layers, namely layer 1, layer 2, and layer 3 with heights of 50 [m], 60 [m], and 70 [m], respectively. Each layer has 30×30 voxels, and the white voxels correspond to the areas in which RSS values are not measured due to the presence of buildings. Consequently, there are 2616 voxels in the RSS map. We use the RSS map as

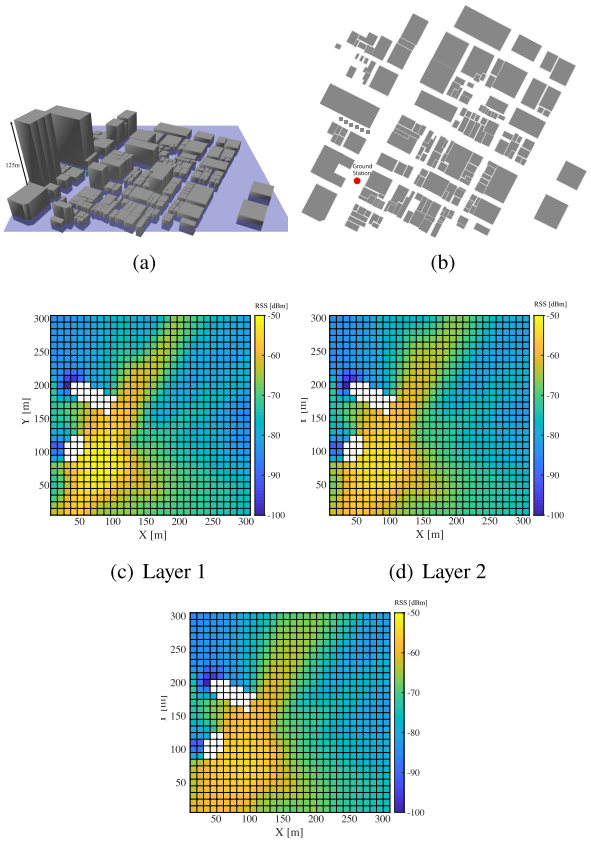

Fig. 8 (a) and (b) show 3D city map used in the simulation experiments). (c), (d), and (e) show the 3D RSS map. The white voxels correspond to buildings, where RSS values are not estimated.

the ground truth to validate the proposed estimator and implement the proposed estimator using MATLAB [41]. To establish the paths, we use the GA solver in the MATLAB global optimization toolbox with a crossover probability of 0.8 and a mutation probability of 0.01. We do not consider the parameter optimization of GA, because it is beyond the scope of this paper. Figure 9 shows examples of the measurement points and the established paths when using the proposed sampling scheme for $H_{\text{th}} = 2, 3$. When $H_{\text{th}} = 2$ and 3, 329 and 167 measurement points are assigned to the voxels, respectively.

In this study, we assume that the UAV can control its position and posture perfectly, and RSS values at measurements points are measured at the centers of the voxels. In practical environments, some errors in the position and posture may occur due to wind disturbance and capability of localization. If the errors exceed the size of each voxel ($10 \times 10 \times 10$ [m^3] in the simulation experiment), they may affect the performance of the proposed estimator and in such a case, the size of each voxel should be set to a larger size. However, the proposed estimator is robust against the errors because it aims at roughly estimating the RSS map.

In the proposed estimator, the 3D-RSS map is estimated by interpolating RSS values with the graph-Laplacian

†The computational cost does not include the cost to obtain matrices in (3) such as $\boldsymbol{F}(m)^{\top}\boldsymbol{F}(m)$.

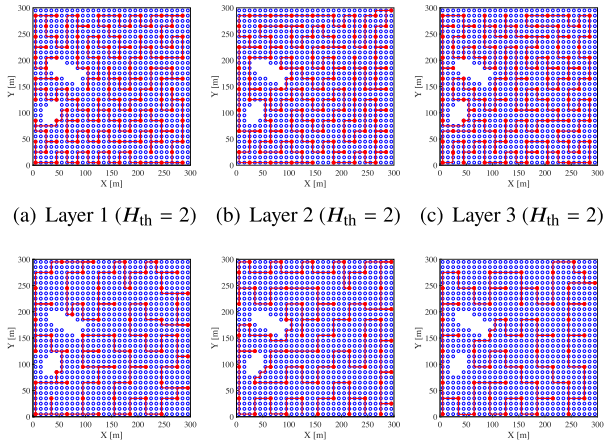

(a) Layer 1 ($H_{\mathrm{th}} = 2$) (b) Layer 2 ($H_{\mathrm{th}} = 2$) (c) Layer 3 ($H_{\mathrm{th}} = 2$)

(d) Layer 1 ($H_{\mathrm{th}} = 3$) (e) Layer 2 ($H_{\mathrm{th}} = 3$) (f) Layer 3 ($H_{\mathrm{th}} = 3$)

Fig. 9 Measurement points and established paths for $H_{\mathrm{th}} = 2$ ((a), (b), and (c)) and $H_{\mathrm{th}} = 3$ ((e), (f), and (g)). The red circles represent the measurement points.

regularized least square estimation. Some techniques use a similar idea such as Kriging-based interpolation [23], [24]. The proposed estimator is different from these techniques in the sense that it estimates the RSS map sequentially. In particular, it cannot obtain the whole RSS map until the node measures RSS values at all measurement points. To the best of our knowledge, no existing method uses a technique similar to that of the proposed estimator. Therefore, we do not compare the performance of the proposed estimator with that of any other method.

In order to evaluate the performance of the estimator, we evaluate the *classes* of vertices. In the 3D-RSS map, we classify each vertex into two classes, and the class $cl(v_n)$ of vertex $v_n \in \mathcal{V}$ is defined as $cl(v_n) = 0$ if $Z(\boldsymbol{c}(q_n)) < P_{\mathrm{th}}$ and $cl(v_n) = 1$ otherwise. In this study, we set $P_{\mathrm{th}} = -70$ [dBm]. We also define the estimated class $\hat{cl}(v_n) = 0$ if $\hat{Z}(\boldsymbol{c}(q_n)) < P_{\mathrm{th}}$ and $\hat{cl}(v_n) = 1$ otherwise. The class estimation error ϵ is given by

$$\epsilon = \sum_{v_n \in \mathcal{V}} \frac{|\hat{cl}(v_n) - cl(v_n)|}{|\mathcal{V}|}.$$

5.2 Simulation Results

Figure 10 shows the 3D-RSS map estimated using the proposed estimator for $H_{\mathrm{th}} = 2$ and $K = 4$. It can be observed that the 3D-RSS map is estimated sequentially, and after the final measurement, the RSS values at all the voxels are estimated. Because the finally obtained RSS maps of all the layers are similar, we will show the RSS map at layer 1 in what follows.

Figure 11 shows the average class estimation error $\bar{\epsilon}$ for $H_{\mathrm{th}} = 2$, $K = 4$ (Fig. 11(a)) and $H_{\mathrm{th}} = 3$, $K = 4$ (Fig. 11(b)). We set the parameters λ and μ to $\lambda = 0.0005, 0.005, 0.05, 0.5, 5$ and $\mu = 0, 0.05, 0.55$, respectively. For a given parameter set of H, K, λ, and μ, $\bar{\epsilon}$ is obtained by

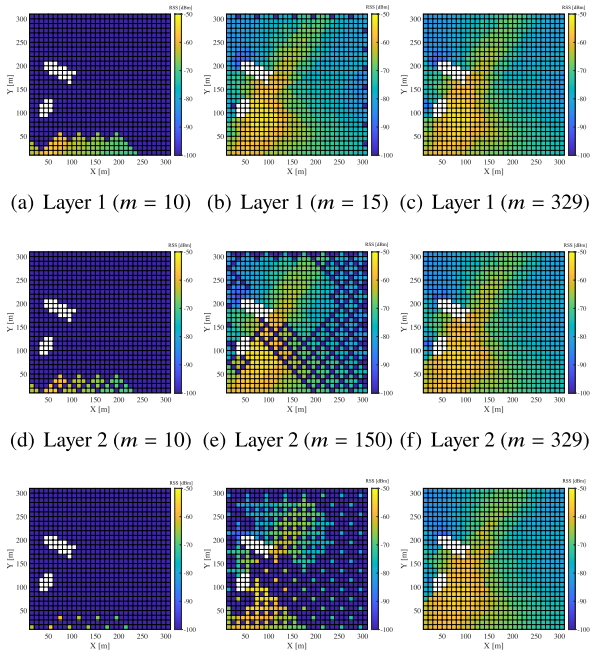

(a) Layer 1 ($m = 10$) (b) Layer 1 ($m = 15$) (c) Layer 1 ($m = 329$)

(d) Layer 2 ($m = 10$) (e) Layer 2 ($m = 150$) (f) Layer 2 ($m = 329$)

(g) Layer 3 ($m = 10$) (h) Layer 3 ($m = 150$) (i) Layer 3 ($m = 329$)

Fig. 10 The 3D-RSS map estimated sequentially using the proposed estimator for $H_{\mathrm{th}} = 2$. The figures on the left ((a), (d), and (g)) show the estimated RSS map after obtaining the 10-th measurement point. The figures in the middle ((b), (e), and (h)) show the estimated RSS map after obtaining the 150-th measurement point. The figures on the right ((c), (f), and (i)) show the estimated RSS map after obtaining the final measurement point (the 329-th measurement point).

$$\bar{\epsilon} = \frac{1}{N_{\mathrm{sim}}} \sum_{i=1}^{N_{\mathrm{sim}}} \epsilon^{(i)},$$

where $\epsilon^{(i)}$ and $N_{\mathrm{sim}} = 10$ denote the class estimation error obtained by the i-th simulation experiment and the number of simulation experiments conducted for each parameter set, respectively. From the figures, it can be seen that the class estimation error is an increasing function of λ for $\lambda > 0.05$. It can also be seen that although the class estimation error is not sensitive to μ for smaller λ, it is considerably affected by μ for larger λ. The reason is that while λ is related to the smoothness of vertices within a measurement graph, μ is related to the smoothness between different measurement graphs. Namely, when μ is small, the estimated 3D-RSS map is not smoothed even with larger λ. On the other hand, when μ is large, a more smoothed 3D-RSS map is obtained because the temporal RSS vectors estimated using different measurement graphs are strongly connected.

Figure 12 shows the estimated RSS maps and classes obtained from the maps for different values of μ. We observe that more smoothed RSS maps and classes are obtained for larger μ. It is difficult to set the parameters in the proposed estimator because the performance of the proposed estimator depends on several factors such as the positions of buildings, the size of the area to be estimated, the number of layers, etc. Because the objective of this paper is to provide an idea of the proposed smooth estimator and

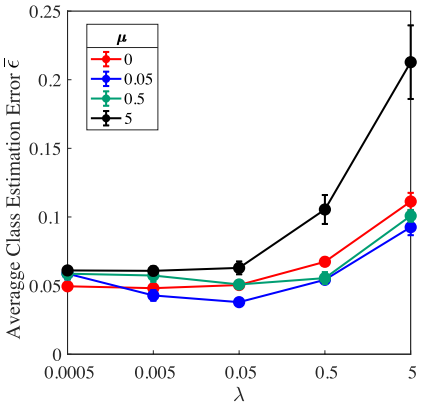

(a) $H_{\text{th}} = 2$

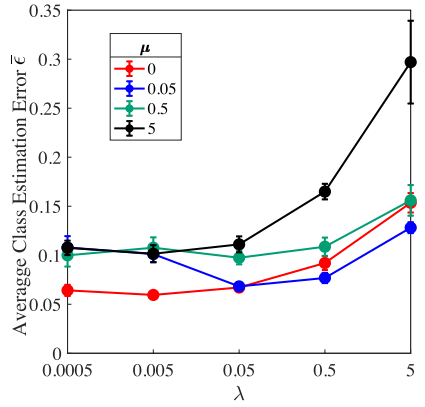

(b) $H_{\text{th}} = 3$

Fig. 11 Average class estimation error $\bar{\epsilon}$ vs. parameter λ for $H_{\text{th}} = 2, 3$. For each plot, the 95% confidence interval is presented.

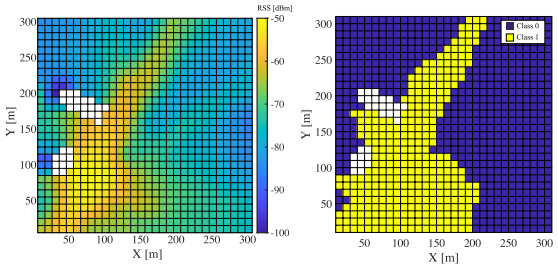

(a) True RSS map (b) True classified RSS map

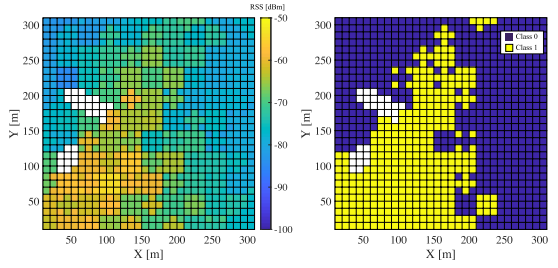

(c) $\mu = 0.$ (d) $\mu = 0.$

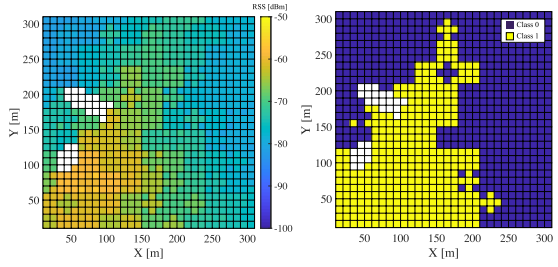

(e) $\mu = 0.05.$ (f) $\mu = 0.05.$

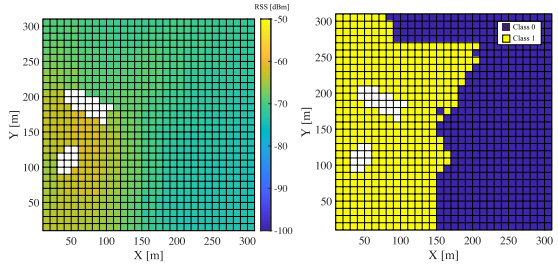

(g) $\mu = 5.$ (h) $\mu = 5.$

Fig. 12 Estimated RSS maps and classes for different values of μ. (a) and (b) show the true RSS map and the classes obtained from the map. (c), (e), (g) show the estimated RSS maps for $\mu = 0, 0.05$, and 5, respectively. (d), (f), and (g) show the estimated classes for $\mu = 0, 0.05$, and 5, respectively.

demonstrate its basic behavior, we do not consider the parameter optimization problem in this paper. However, it is worth mentioning that the parameters, λ and μ, rely on parameters K and H_{th}. Larger K and/or smaller H_{th} result in constructing larger measurement graphs. From the discussion in Fig. 11, λ and μ affect the smoothness within a measurement graph and between measurement graphs, respectively. Therefore, for a given three-dimensional area, λ is more important for larger measurement graphs and μ is more important for smaller ones. Furthermore, the number of classes, where two classes (i.e., $cl(v_n) \in \{0, 1\}$) are considered in this study, also affects the parameter setting. Because a more smoothed RSS map is estimated with larger μ, smaller μ should be used to evaluate the RSS map with finer resolution of more than two classes.

In the true 3D-RSS map used in the simulation experiments, all three layers have similar spatial distributions of RSS values, and therefore, almost all temporal graphs (except a measurement time when the UAV moves to an upper layer) are constructed by measurement points on the same layer. Although we leave the performance evaluation regarding environments where the layers have different spatial distributions for the future work, we consider that the proposed estimator can be applied to such an environment by constructing temporal graphs including measurement points on different layers.

6. Conclusion

In this study, we considered a 3D-RSS map for ground-to-air wireless communication and proposed a graph Laplacian-based sequential smooth estimator for the 3D-RSS map. In the proposed estimator, a UAV measures the RSS values at positions along an established path and a measurement graph is constructed dynamically according to the measure-

ment points. By performing graph-Laplacian regularized least square estimation, the 3D-RSS map is sequentially estimated. Through simulation experiments, we showed that the proposed estimator can obtain a smooth estimation of the 3D-RSS map with much fewer measurement points than the number of voxels in the 3D-RSS map.

In this study, we focused on the case in which there is one UAV and one ground station. When there are multiple UAVs and ground stations, we need to consider the path establishment problem for UAVs to efficiently estimate the 3D-RSS map. Furthermore, in this study, we did not consider the battery consumption problem; we assumed that the UAV could obtain all measurements without the battery constraint. This problem is also related to the path establishment problem. We will study these problems in the future work.

Acknowledgments

This work was supported in part by the Grants-in-Aid for Scientific Research (B) from Japan Society for the Promotion of Science (JSPS) under Grant JP18H01445 and Grant JP19H04096, Adaptable and Seamless Technology transfer Program through Target-driven R&D (A-STEP) from Japan Science and Technology Agency (JST) (No. JPMJTM19F3), the Japanese Ministry of Internal Affairs and Communications in R&D on Cooperative Technologies and Frequency Sharing Between Unmanned Aircraft System (UAS)-Based Wireless Relay Systems and Terrestrial Networks, and TMU local 5G research support.

References

[1] Y. Zeng, J. Lyu, and R. Zhang, "Cellular-connected UAV: Potential, challenges, and promising technologies," IEEE Wireless Commun., vol.26, no.1, pp.120–127, Feb. 2019.
[2] A. Fotouhi, M. Ding, and M. Hassan, "Flying drone base stations for macro hotspots," IEEE Access, vol.6, pp.19530–19539, March 2018.
[3] J. Plachy, Z. Becvar, P. Mach, R. Marik, and M. Vondra, "Joint positioning of flying base stations and association of users: Evolutionary-based approach," IEEE Access, vol.7, pp.11454–11463, Jan. 2019.
[4] W. Shi, J. Li, W. Xu, H. Zhou, N. Zhang, S. Zhang, and X. Shen, "Multiple drone-cell deployment analyses and optimization in drone assisted radio access networks," IEEE Access, vol.6, pp.12518–12529, Feb. 2018.
[5] F. Al-Turjman, J.P. Lemayian, S. Alturjman, and L. Mostarda, "Enhanced deployment strategy for the 5G drone-BS using artificial intelligence," IEEE Access, vol.7, pp.75999–76008, June 2019.
[6] I. Bekmezci, O.K. Sahingoz, and S. Temel, "Flying ad-hoc networks (FANETs): A survey," Ad Hoc Networks, vol.11, no.3, pp.1254–1270, May 2013.
[7] Y.J. Chen and D.Y. Huang, "Trajectory optimization for cellular-enabled UAV with connectivity outage constraint," IEEE Access, vol.8, pp.29205–29218, Feb. 2020.
[8] T. Matsuda, M. Kaneko, T. Hiraguri, K. Nishimori, T. Kimura, and A. Nakao, "Adaptive direction control for UAV full-duplex relay networks using multiple directional antennas," IEEE Access, vol.8, pp.85083–85093, May 2020.
[9] R. Amorim, I.Z. Kovacs, J. Wigard, G. Pocovi, T.B. Sorensen, and P. Mogensen, "Improving drone's command and control link reliability through dual-network connectivity," Proc. 2019 IEEE 89th Veh. Technol. Conf., pp.1–6, IEEE, April 2019.
[10] N. Goddemeier and C. Wietfeld, "Investigation of air-to-air channel characteristics and a UAV specific extension to the Rice model," Proc. 2015 IEEE GLOBECOM Work. (GC Wkshps), pp.1–5, IEEE, Dec. 2015.
[11] C. Yan, L. Fu, J. Zhang, and J. Wang, "A comprehensive survey on UAV communication channel modeling," IEEE Access, vol.7, pp.107769–107792, Aug. 2019.
[12] W. Khawaja, I. Guvenc, D.W. Matolak, U.C.C. Fiebig, and N. Schneckenburger, "A survey of air-to-ground propagation channel modeling for unmanned aerial vehicles," IEEE Commun. Surveys Tuts., vol.21, no.3, pp.2361–2391, Third Quater 2019.
[13] A.A. Khuwaja, Y. Chen, N. Zhao, M.S. Alouini, and P. Dobbins, "A survey of channel modeling for UAV communications," IEEE Commun. Surveys Tuts., vol.20, no.4, pp.2804–2821, Fourth Quater 2018.
[14] E. Yanmaz, R. Kuschnig, and C. Bettstetter, "Channel measurements over 802.11a-based UAV-to-ground links," Proc. 2011 IEEE GLOBECOM Work. (GC Wkshps), pp.1280–1284, Dec. 2011.
[15] R. Amorim, H. Nguyen, P. Mogensen, I.Z. Kovacs, J. Wigard, and T.B. Sorensen, "Radio channel modeling for UAV communication over cellular networks," IEEE Wirel. Commun. Lett., vol.6, no.4, pp.514–517, Aug. 2017.
[16] A. Al-Hourani and K. Gomez, "Modeling cellular-to-UAV path-loss for suburban environments," IEEE Wirel. Commun. Lett., vol.7, no.1, pp.82–85, Feb. 2018.
[17] E. Yanmaz, R. Kuschnig, and C. Bettstetter, "Achieving air-ground communications in 802.11 networks with three-dimensional aerial mobility," Proc. IEEE INFOCOM, pp.120–124, April 2013.
[18] F. Jiang and A.L. Swindlehurst, "Optimization of UAV heading for the ground-to-air uplink," IEEE J. Sel. Areas Commun., vol.30, no.5, pp.993–1005, June 2012.
[19] J. Pang and G. Cheung, "Graph Laplacian regularization for image denoising: Analysis in the continuous domain," IEEE Trans. Image Process., vol.26, no.4, pp.1770–1785, April 2017.
[20] X. Liu, D. Zhai, D. Zhao, G. Zhai, and W. Gao, "Progressive image denoising through hybrid graph Laplacian regularization: A unified framework," IEEE Trans. Image Process., vol.23, no.4, pp.1491–1503, April 2014.
[21] M. Lopez, T.B. Sorensen, P. Mogensen, J. Wigard, and I.Z. Kovacs, "Shadow fading spatial correlation analysis for aerial vehicles: Ray tracing vs. measurements," Proc. 2019 IEEE 90th Veh. Technol. Conf., pp.1–5, Sept. 2019.
[22] S.S. Szyszkowicz, H. Yanikomeroglu, and J.S. Thompson, "On the feasibility of wireless shadowing correlation models," IEEE Trans. Veh. Technol., vol.59, no.9, pp.4222–4236, Nov. 2010.
[23] A.B.H. Alaya-Feki, S.B. Jemaa, B. Sayrac, P. Houze, and E. Moulines, "Informed spectrum usage in cognitive radio networks: Interference cartography," Proc. 2008 IEEE 19th Int. Symp. Pers. Indoor Mob. Radio Commun., (PIMRC 2008) pp.1–5, Sept. 2008.
[24] K. Sato and T. Fujii, "Kriging-based interference power constraint: Integrated design of the radio environment map and transmission power," IEEE Trans. Cogn. Commun. Netw., vol.3, no.1, pp.13–25, March 2017.
[25] J.A. Bazerque, G. Mateos, and G.B. Giannakis, "Group-lasso on splines for spectrum cartography," IEEE Trans. Signal Process., vol.59, no.10, pp.4648–4663, Oct. 2011.
[26] B.A. Jayawickrama, E. Dutkiewicz, I. Oppermann, G. Fang, and J. Ding, "Improved performance of spectrum cartography based on compressive sensing in cognitive radio networks," Proc. ICC 2013, pp.5657–5661, June 2013.
[27] D. Romero, S.j. Kim, G.B. Giannakis, and R. Lopez-Valcarce, "Learning power spectrum maps from quantized power measurements," IEEE Trans. Signal Process., vol.65, no.10, pp.2547–2560, May 2017.

[28] J. Chen, U. Yatnalli, and D. Gesbert, "Learning radio maps for UAV-aided wireless networks: A segmented regression approach," Proc. IEEE ICC 2017, pp.1–6, May 2017.
[29] O. Esrafilian and D. Gesbert, "3D city map reconstruction from UAV-based radio measurements," Proc. IEEE GLOBECOM 2017, pp.1–6, Dec. 2017.
[30] H. Nishioka, A. Danjo, S. Hara, T. Matsuda, F. Ono, R. Miura, and F. Kojima, "A compressed sensing-based 3D-RSS MAP completion for UAV routes planning," Proc. 2018 12th Int. Conf. Sens. Technol., pp.273–277, Dec. 2018.
[31] Y. Mostofi, "Compressive cooperative sensing and mapping in mobile networks," IEEE Trans. Mobile Comput., vol.10, no.12, pp.1769–1784, Dec. 2011.
[32] E. Candes and M. Wakin, "An introduction to compressive sampling," IEEE Signal Process. Mag., vol.25, no.2, pp.21–30, March 2008.
[33] S. Gandy, B. Recht, and I. Yamada, "Tensor completion and low-n-rank tensor recovery via convex optimization," Inverse Probl., vol.27, no.2, p.025010, Feb. 2011.
[34] D.I. Shuman, S.K. Narang, P. Frossard, A. Ortega, and P. Vandergheynst, "The emerging field of signal processing on graphs: Extending high-dimensional data analysis to networks and other irregular domains," IEEE Signal Process. Mag., vol.30, no.3, pp.83–98, May 2013.
[35] F. Chung, Spectral Graph Theory, CBMS Regional Conference Series in Mathematics, vol.92, American Mathematical Society, Dec. 1996.
[36] J.L. Gross, J. Yellen, and P. Zhang, Handbook of Graph Theory, Chapman and Hall/CRC, Dec. 2013.
[37] D.A. Harville, Matrix Algebra From a Statistician's Perspective, Springer, 1997.
[38] B. Korte and J. Vygen, Combinatorial Optimization, 5th ed., Algorithms and Combinatorics, vol.21, Springer, 2012.
[39] T.H. Cormen, C.E. Leiserson, R.L. Rivest, and C. Stein, Introduction to Algorithms, 2nd ed., MIT press, 2001.
[40] WinProp, https://altairhyperworks.com/product/FEKO/WinProp-Propagation-Modeling, Altair Engineering, Inc.
[41] MATLAB, https://www.mathworks.com/, The MathWorks, Inc.

Takahiro Matsuda received his B.E. with honors, M.E., and Ph.D. degrees in communications engineering from Osaka University in 1996, 1997, 1999, respectively. He joined the Department of Communications Engineering at the Graduate School of Engineering, Osaka University in 1999. In the same department, he was an Assistant Professor from 1999 to 2005, a Lecturer from 2005 to 2009, and an Associate Professor from 2009 to 2018. He is currently a Professor in the Department of Computer Science, Graduate School of Systems Design, Tokyo Metropolitan University. His research interests include performance analysis and the design of communication networks and wireless communications. He received the Best Tutorial Paper Award and the Best Magazine Paper Award from IEICE ComSoc in 2012, and the Best Paper Award from IEICE in 2014. He is a member of IPSJ and IEEE.

Fumie Ono received her B.E., M.E., and Ph.D. degrees in electrical engineering from Ibaraki University, in 1999, 2001, 2004, respectively. She worked as a research associate with the Faculty of Engineering, Tokyo University of Science, from 2004 to 2006. From 2006 to 2011, she was an assistant professor at the Division of Electrical and Computer Engineering, Yokohama National University. Since 2012, she has been with National Institute of Information and Communications Technology (NICT) as a senior researcher. She is currently seconded from NICT to Ministry of Internal Affairs and Communications. She is a member of IEEE and IEICE.

Shinsuke Hara received his B.Eng., M.Eng., and Ph.D. degrees in communications engineering from Osaka University, Osaka, Japan, in 1985, 1987, and 1990, respectively. He was an Assistant Professor from April 1990 to September 1997 and an Associate Professor from October 1997 to September 2005 at Osaka University. Since October 2005, he has been with the Graduate School of Engineering, Osaka City University as a Professor. From April 1995 to March 1996, he also worked as a visiting scientist at the Telecommunications and Traffic Control Systems Group, Delft University of Technology, Delft, The Netherlands. His research interests include mobile and indoor wireless communications and digital signal processing.